Macromolecules

pubs.acs.org/Macromolecules Article

Single-Ion-Conducting Polyether Electrolytes via Orthogonal Postpolymerization Modification

Jiyoung Lee, Seonho Kim, Hyeoksu Kwon, Seungyun Jo, Du Yeol Ryu, U Hyeok Choi,* and Byeong-Su Kim*

Cite This: https://doi.org/10.1021/acs.macromol.3c00985 Read Online

ACCESS | Metrics & More | Article Recommendations | Supporting Information

ABSTRACT: Solid polymer electrolytes are considered promising alternatives for overcoming the safety issues of conventional liquid electrolytes. In particular, poly(ethylene oxide)-based polymer electrolytes are widely studied because of their high flexibility and ion-solvating capability but suffer from low ionic conductivity at room temperature due to high crystallinity of poly(ethylene oxide) restricting segmental motion. To address this challenge, we present a new type of polyether-based single-ion-conducting solid polymer electrolyte whose constituent functional groups can be tailored in an orthogonal manner. The electrolyte structure was designed to possess weakly binding anionic and flexible lithium-cation-solvating pendants along the polyether backbone. Specifically, bulk polymerization between allylamine and diepoxide was employed to synthesize the polyether backbone with functional allyl and hydroxyl groups. The resulting polymer was subsequently further functionalized with lithium bis(trifluoromethanesulfonyl)imide and tri(ethylene glycol) groups to create a single-ion conductor. Tri(ethylene glycol) promoted segmental α and ion-rearranging α_2 relaxations (arising from a lowered glass transition temperature and increased ion mobility, μ) as well as increased the dielectric constant (leading to a large number density of conducting ions, p), resulting in a significant increase in the ionic conductivity ($\sigma \sim \mu p$), e.g., a 250-fold increase at 60 °C. Furthermore, addition of succinonitrile (a plasticizer) increased the ionic conductivity of the single-ion-conducting solid polymer electrolyte to 1.8×10^{-5} S cm^{-1} at 60 °C because of a weakened ion−ion correlation as revealed by wide-angle X-ray scattering analyses. These results demonstrate the potential of tailoring properties of solid polymer electrolytes by introducing various functional moieties.

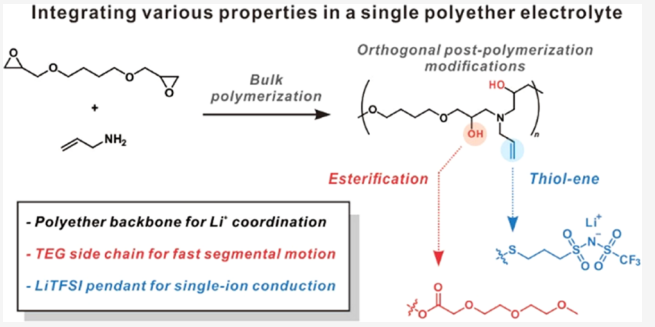

INTRODUCTION

Lithium-ion batteries (LIBs) are widely used for energy storage systems owing to their high energy density, high charge/discharge rate, lightweight, and long service life. The currently available commercial LIBs employ liquid electrolytes consisting of a lithium salt dissolved in an organic solvent.[1,2] Although liquid electrolytes exhibit an excellent wettability, a low charge-transfer interfacial resistance, and a high ionic conductivity ($\geq 10^{-3}$ S cm^{-1}) at room temperature,[3,4] they are flammable, leak-prone, and corrosive. Moreover, the electrode/liquid electrolyte interface is thermodynamically unstable and reactive, and thus, it induces lithium dendrite growth and limits the use of such electrolytes at high temperatures.[5−7] Therefore, it is necessary to develop next-generation electrolytes that can circumvent the aforementioned safety issues while maintaining high ionic conductivity and capacity.

Solid polymer electrolytes (SPEs) have emerged as promising alternative electrolytes because of their flame-resistance, small volume variation during operation, and high-temperature durability.[8,9] SPEs are generally composed of a polymer containing Lewis bases, such as ether or carbonyl groups, and a lithium salt (e.g., lithium bis(trifluoromethanesulfonyl)imide (LiTFSI)).[10] However, conventional SPEs, in which both cations and anions are mobile, are characterized by a low lithium-ion transference number ($t_{Li^+} < 0.5$) that induces concentration polarization, resulting in dendrite penetration, a limited power density, and a poor cycling performance.[11,12] Therefore, a single-ion conduction system that can selectively transport lithium cation (Li^+) was devised to prevent concentration polarization, oxidation of counteranions, and lithium dendrite growth. Single-ion-conducting SPEs (SISPEs) are mainly achieved through covalent attachment of a bulky anion, which allows charge delocalization onto the polymer backbone.[13,14] Armand and co-workers reported the blend and block copolymer based on

Received: May 19, 2023
Revised: August 20, 2023

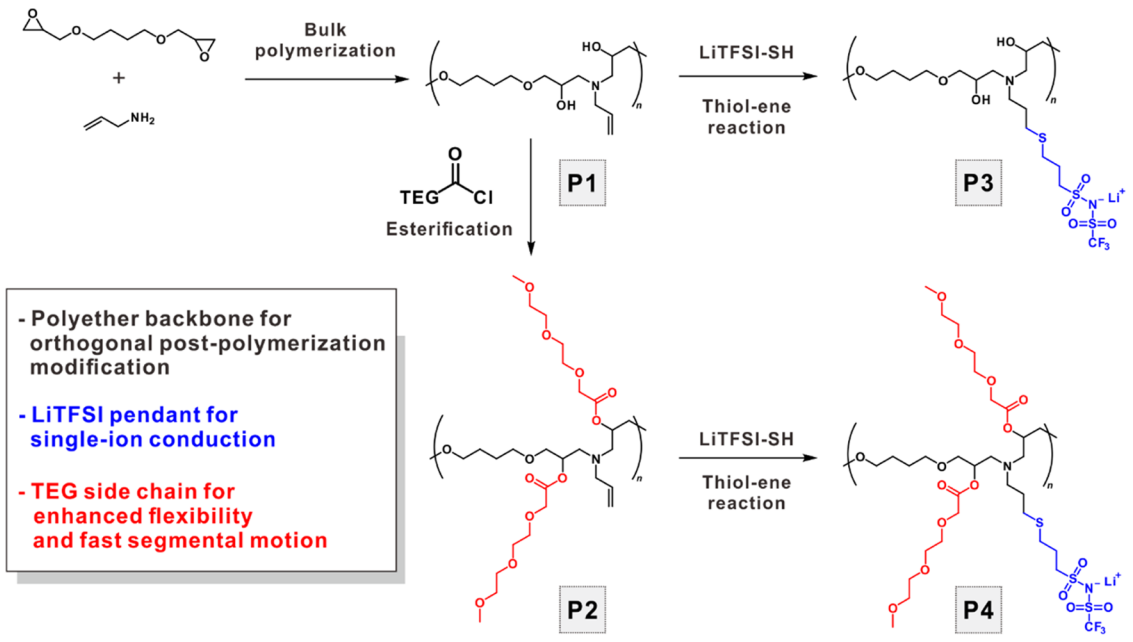

Figure 1. Schematic illustration of the SISPEs subjected to orthogonal postpolymerization modification (TEG: tri(ethylene glycol) and LiTFSI: lithium bis(trifluoromethanesulfonyl)imide).

poly(styrene trifluoromethanesulfonylimide of lithium) (P(STFSILi)), in which sulfonylimide-based anionic groups were chemically attached to polystyrene chains. In particular, the block copolymer of P(STFSILi)−poly(ethylene oxide) (PEO)−P(STFSILi) exhibited a high t_{Li^+} of 0.85 and an excellent ionic conductivity of 1.3×10^{-5} S cm^{-1} at 60 °C.[15,16]

PEO-based SPEs have been extensively studied owing to their excellent Li^+ solubility and chain flexibility.[9,17] The Li^+ conduction in PEO-based SPEs primarily occurs through segmental motion of the lithium-coordinated polymer chains in the amorphous state.[17,18] However, below the melting point, segmental motion of PEO-based SPEs is significantly restricted.[19,20] The crystalline phase that forms below the melting point exhibits lower conductivity due to the high energy barrier required for the cooperative motion of Li^+ between the preferred sites.[21] As a result, the segmental motion is apparent only at temperatures exceeding the glass-transition temperature (T_g) of PEO-based SPEs, making it challenging to achieve an adequate ionic conductivity of at least 10^{-3} S cm^{-1} at ambient temperature necessary for practical applications. To date, various strategies, such as the introduction of flexible functional groups (e.g., postpolymerization or block copolymerization), to enhance the segmental dynamics of polymer electrolytes have been reported. For example, Lee's group reported SPEs based on tri(ethylene glycol) (TEG)-substituted polyether.[22] The TEG group reduced the crystallinity of the polymer and improved Li^+ transport. As a result, the room-temperature ionic conductivity of the TEG-containing SPEs was improved more than that of the PEO-based electrolytes, and the ionic conductivity of these TEG-containing SPEs did not show any abrupt decay at low temperatures. Moreover, a series of vinyl ether-based PEO side chain copolymer electrolytes was investigated.[23] Copolymers with long PEO side chains and high grafting densities exhibit a low glass transition temperature (T_g) and thus high ionic conductivity.

Furthermore, to immobilize anions and enhance segmental motion, SISPEs with weakly binding ionic and flexible polar functional groups have been demonstrated. For example, Thelakkat and Krimalowski incorporated bistriflimide anion ($TFSI^-$), TEG, and benzyl groups into a polyether-based backbone via sequential copper-mediated click reactions.[24] However, because the functionalization was realized by a one-pot synthesis, it was difficult to control the ratio of the functional groups introduced into the polymer. Meanwhile, Mecerreyes group reported a family of SISPEs based on delocalized borate groups, which were synthesized by free radical polymerization of multifunctional monomers.[25] However, the synthesis of monomers requires a multistep reaction under inert conditions. To control the characteristics of SISPEs effectively, a new platform that can simplify the introduction of several functional groups, such as flexible Li^+ solvating groups and strongly delocalized ionic groups, is required; such a platform is necessary to promote the dissociation and transportation of Li^+ as well as control the ratio of functional groups.

Herein, we present the design and synthesis of polyether-based SISPEs by exploiting the polymer backbone that can introduce diverse functional moieties through orthogonal functionalization (Figure 1). To prepare SISPEs with improved segmental motion, $TFSI^-$ and TEG groups were introduced to the polyether backbone bearing allyl and hydroxyl groups. The ionic conductivity of the SISPE bearing the TEG group was approximately 250 times higher than that of the SISPEs with no TEG group at 60 °C. Incorporation of succinonitrile (SN), a plasticizer, into the SISPE further enhanced its ionic conductivity to the order of 1.8×10^{-5} S cm^{-1} at 60 °C. Using dielectric relaxation spectroscopy (DRS), differential scanning calorimetry (DSC), and wide-angle X-ray scattering (WAXS), the ion and polymer dynamics of SISPE were analyzed over a broad range of frequencies and temperatures. The corresponding results provided insights into the structure−property relationships in terms of ionic conductivity, relaxation processes, T_g, and dielectric constant. According to DRS analysis, the incorporated TEG group accelerated the α and α_2 relaxations and increased the static dielectric constant.

https://doi.org/10.1021/acs.macromol.3c00985
Macromolecules XXXX, XXX, XXX−XXX

This result was consistent with that of a physical model of electrode polarization (EP), which indicated an increase in the conducting ion mobility and concentration. Furthermore, the WAXS analysis revealed a weakened ion−ion correlation upon the addition of SN, suggesting that the ion pairs observed in the host SISPE were solvated by SN, thus boosting Li^+ conduction.

EXPERIMENTAL SECTION

Materials. All of the reagents and solvents used in this study were purchased from commercial chemical suppliers (Sigma-Aldrich, TCI Chemicals, Thermo Fisher Scientific, Alfa Aesar, and SAMCHUN Chemicals), unless otherwise stated. Deuterated MeOD-d_4 and D_2O NMR solvents were purchased from Cambridge Isotope Laboratories. Tetrahydrofuran (THF) and *N*,*N*-dimethylformamide (DMF) were dried and degassed using a solvent purifier (Vacuum Atmospheres) and used immediately after collection. Triethylamine was distilled under nitrogen over CaH_2, and allylamine was distilled under nitrogen over $CaCl_2$.

Characterization. ^{1}H and correlation spectroscopy (COSY) NMR spectra were recorded on a Bruker 400 MHz spectrometer at 25 °C. Chemical shifts are reported in ppm relative to the signals corresponding to the residual nondeuterated solvents: $CDCl_3$, δH = 7.26 ppm; MeOD-d_4, δH = 3.31 ppm; D_2O, δH = 4.79 ppm. Fourier transform infrared (FT-IR) spectra were recorded on an Agilent Cary 630 spectrometer with an attenuated total reflection (ATR) module. The number-average (M_n) and weight-average (M_w) molecular weights and the corresponding molecular-weight distributions (M_w/M_n, $Đ$) were measured by gel permeation chromatography (GPC) using an Agilent 1260 series system, with DMF as an eluent, at 25 °C and a flow rate of 1.00 mL min^{-1} using a refractive index (RI) detector. All of the calibrations were performed by using poly(methyl methacrylate) (PMMA) standards (Sigma-Aldrich; M_p 500−2,700,000). Differential scanning calorimetry (DSC) (Q200 model, TA Instruments) measurements were performed under a nitrogen atmosphere from −80 to 150 °C at a heating rate of 10 °C min^{-1}. Before the measurements, the sample was annealed, and the second cycle was used to determine the thermal properties of the resulting polymers. Thermogravimetric analysis (TGA) was performed under a nitrogen atmosphere using a TGA Q50 analyzer (TA Instruments) from 30 to 1000 °C at a heating rate of 10 °C min^{-1}. The ionic conductivity and complex permittivity measurements were conducted using a Novocontrol GmbH Concept 40 broadband dielectric relaxation spectrometer and Bio-Logic Science Instruments impedance spectroscopy system (VSP300). The samples were prepared by sandwiching the polymer between two polished brass electrodes with two different diameters of 30 mm (top electrode) and 40 mm (bottom electrode). The lithium-ion transference number (t_{Li^+}) was measured by fabricating a Li symmetric cell (Li/P4/Li). For the preparation of the CR-2032-type Li symmetric coin cell, a mixture solution of P4 and propylene carbonate in a weight ratio of 1:1 and a polypropylene separator were applied to prevent short circuit. Wide-angle X-ray scattering (WAXS) measurements were performed at the 9A beamlines in the Pohang Accelerator Laboratory, Korea. The operating conditions for the WAXS measurements were well optimized for the structural analyses: wavelength of 1.12 Å, sample-to-detector distance of 0.2 m, beam energy of 11.08 keV, beam size of 0.030 × 0.290 mm^2, and exposure time of 10 s. The WAXS patterns were collected by a 2D detector (SX-165, Rayonix) at the end of a vacuum guide tube. Density functional theory (DFT) calculations were performed using the DMol3 module available in Materials Studio 2023 from BIOVIA. The structures of P3 and P4 were optimized using Perdew−Burke−Ernzerhof (PBE)[26] functionals and the generalized gradient approximation (GGA) method. The convergence tolerance of energy and SCF tolerance were set at 2 × 10^{-5} Ha and 10^{-5}, respectively. The binding energies of Li^+TFSI^- in the SISPEs were adjusted for the basis set superposition error (BSSE) using the counterpoise correction technique.

Synthesis of P1. P1 was synthesized using a previously reported method with modifications.[27] Allylamine (7.5 mL, 0.10 mol) and 1,4-butanediol diglycidyl ether (18 mL, 0.10 mol) were placed in a 500 mL round-bottomed flask in a 1:1 molar ratio and stirred using a mechanical stirrer at room temperature for 48 h. The crude polymeric mixture was dissolved in methanol and precipitated twice in diethyl ether. The polymer solution was concentrated *in vacuo* to obtain P1 as a colorless oil (97% yield). ^{1}H NMR (400 MHz, MeOD-d_4): δ (ppm) 5.89−5.82 (m, 1H), 5.17−5.10 (t, 2H), 3.81−3.78 (m, 2H), 3.44−3.31 (m, 8H), 3.20−3.10 (m, 2H), 2.64−2.45 (m, 4H), 1.61 (s, 4H). GPC (DMF): M_n = 10,000 g mol^{-1}, M_w = 24,000 g mol^{-1}, and $Đ$ (M_w/M_n) = 2.32.

Synthesis of LiTFSI-SH. LiTFSI-SH was synthesized using a previously reported method.[28]

Synthesis of LiTFSI-allyl. All of the reactions were carried out under a nitrogen atmosphere. A mixture of oxalyl chloride (2.4 mL, 28 mmol) in 30 mL of acetonitrile and 0.50 mL of DMF was stirred at room temperature for 1 h, and a small amount of sodium allyl sulfonate (3.1 g, 22 mmol) was added to this mixture at 0 °C. The solution was stirred for 3 h at 0 °C and again for 2 h at room temperature. Trifluoromethanesulfonamide (3.2 g, 21 mmol) and anhydrous lithium hydroxide (0.56 g, 22 mmol) were added to an ice−water bath, and the mixture was stirred at room temperature for 24 h. The residue was filtered off and purified using column chromatography (ethyl acetate/methanol, 10/1 v/v). The product was concentrated *in vacuo* to obtain a white solid (24% yield). ^{1}H NMR (400 MHz, D_2O): δ (ppm) 5.99−5.90 (m, 1H), 5.52 (dd, 2H), 4.00 (d, 2H).

Synthesis of LiTFSI-thioester. The prepared LiTFSI-allyl monomer (1.4 g, 5.3 mmol), 2,2-dimethoxy-2-phenylacetophenone (DMPA) (2.7 g, 11 mmol), and thioacetic acid (2.2 mL, 32 mmol) were dissolved in methanol and degassed by nitrogen. The mixture was then irradiated by UV light at room temperature for 16 h to induce a thiol−ene reaction. The solvents were evaporated *in vacuo*, and the excess thioacetic acid and DMPA were removed by dissolving the crude material in diethyl ether to yield a white solid product (68% yield). ^{1}H NMR (400 MHz, D_2O): δ (ppm) 3.31−3.28 (m, 2H), 3.02−2.98 (t, 2H), 2.35 (s, 3H), 2.12−2.05 (m, 2H).

Synthesis of LiTFSI-SH. The LiTFSI-thioester monomer (1.2 g, 3.6 mmol) and 35 wt % aqueous HCl (0.63 mL, 7.2 mmol) were mixed with methanol and stirred at 60 °C for 16 h for hydrolysis. The final product was obtained after neutralization with an aqueous solution of lithium hydroxide, followed by solvent removal (90% yield). ^{1}H NMR (400 MHz, D_2O): δ (ppm) 3.41−3.31 (t, 2H), 2.67−2.64 (t, 2H), 2.10−2.06 (m, 2H).

Synthesis of P2. P2 was synthesized under a nitrogen atmosphere by following a previously reported protocol with modifications.[27,29] In this process, 2-[2-(2-methoxyethoxy)ethoxy]acetyl chloride was prepared by stirring a solution of 2-[2-(2-methoxyethoxy)ethoxy]-acetic acid (5.0 g, 28 mmol) and oxalyl chloride (5.9 g, 47 mmol) in 3.0 mL of toluene for 4 h at 65 °C. The solvent and excess reagent were removed in vacuo, and the residue was used without further purification. P1 (2.2 g, 8.5 mmol for the hydroxyl group) was dissolved in dry THF and stirred in an ice−water bath for 5 min. Then, triethylamine (5.2 g, 51 mmol) and *N*,*N*-dimethylaminopyridine (DMAP), a catalyst, were added, and the mixture was stirred for 10 min. Next, 2-[2-(2-methoxyethoxy)ethoxy]acetyl chloride was added dropwise. The final mixture was stirred at 25 °C for 12 h, and the solution was filtered and concentrated in vacuo. After the reaction mixture was extracted to remove aqueous impurities and the DMAP catalyst with dichloromethane, the organic layer was dried over anhydrous sodium sulfate and concentrated *in vacuo*. The polymer was precipitated twice in hexane and finally dried. The resulting polymer was obtained as a yellow oil (74% yield). ^{1}H NMR (400 MHz, MeOD-d_4): δ (ppm) 5.81−5.74 (m, 1H), 5.19−5.11 (m, 4H), 4.15 (s, 4H), 3.63−3.36 (m, 24H), 3.33 (s, 6H), 3.22−3.15 (m, 2H), 2.68−2.64 (m, 4H), 1.58 (s, 4H). GPC (DMF): M_n = 24,000 g mol^{-1}, M_w = 48,000 g mol^{-1}, $Đ$ (M_w/M_n) = 1.96.

Synthesis of P3 and P4. P3 and P4 were synthesized using a previously reported procedure with modifications.[27,28] P1 or P2 (2.0

https://doi.org/10.1021/acs.macromol.3c00985
Macromolecules XXXX, XXX, XXX−XXX

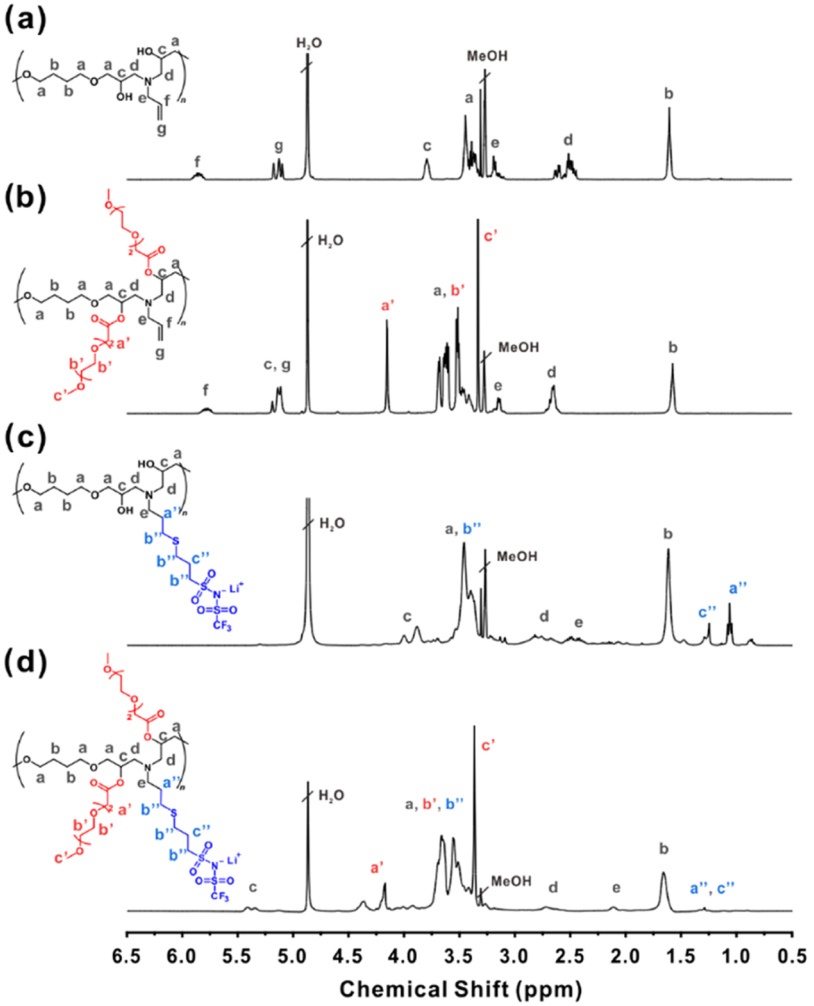

Figure 2. ^{1}H NMR spectra (400 MHz, MeOD-d_4) of (a) P1, (b) P2, (c) P3, and (d) P4 with their corresponding chemical structures.

mmol for the allyl group), LiTFSI-SH (1.8 g, 6.0 mmol), and DMPA (0.32 g, 1.2 mmol) were dissolved in 50 mL of methanol, and the reaction mixture was deoxygenated via nitrogen bubbling. The reaction was continued for 2 h under UV light irradiation (λ = 365 nm), until all of the allyl peaks in the ^{1}H NMR spectra disappeared. Subsequently, the solvent was removed *in vacuo*. The obtained crude polymer was dialyzed against methanol (molecular-weight cutoff (MWCO) 1000 Da dialysis membrane, Fisher Scientific) for 2 days, after which the purified polymer was concentrated and stored at room temperature. The resulting P3 and P4 were obtained as white and yellow rubbery solids (P3: 37% yield and P4: 24% yield).

P3: ^{1}H NMR (400 MHz, MeOD-d_4): δ (ppm) 4.00−3.88 (m, 2H), 3.60−3.09 (m, 14H), 2.85−2.68 (m, 4H), 2.53−2.42 (m, 2H), 1.62 (m, 4H), 1.29−1.25 (m, 2H), 1.07 (m, 2H).

P4: ^{1}H NMR (400 MHz, MeOD-d_4): δ (ppm) 5.41−5.35 (m, 2H), 4.38−4.14 (m, 4H), 3.70−3.31 (m, 36H), 2.94−2.57 (m, 4H), 2.20−2.04 (m, 2H), 1.66 (s, 4H), 1.34−1.07 (m, 4H).

RESULTS AND DISCUSSION

Synthesis and Characterization of SISPEs. A series of SISPEs were prepared in two steps: (1) synthesis of the polymer backbone and (2) postpolymerization modification with the two functional pendants (see Figure S1 in the Supporting Information). The synthesis of polymer backbone (P1) was conducted via bulk polymerization of allylamine and 1,4-butanediol diglycidyl ether at 25 °C for 2 days following a literature protocol with modifications.[27] One advantageous aspect of the synthetic approach lies in its versatility in preparing a flexible polymeric backbone with diverse functionalities. By combination of different functional amines and diepoxides, a wide range of polymers can be prepared, each offering unique functionalities. In this study, P1 has two orthogonal reactive sites, viz. allyl and hydroxyl groups. TEG and TFSI$^-$ groups were introduced via esterification and thiol−ene reaction, respectively. To avoid side reactions during the postpolymerization, 2-[2-(2-methoxyethoxy)ethoxy]acetyl chloride and LiTFSI-SH (Figure S2) were added in 3 equiv with respect to the hydroxyl and allyl groups, respectively. P2 and P3 were functionalized with TEG and TFSI$^-$, respectively, whereas both TFSI$^-$ and TEG were introduced into P4. To eliminate any residual reactants, extensive purification steps were performed. Extraction and precipitation methods were employed to remove 2-[2-(2-methoxyethoxy)ethoxy]acetyl chloride, while dialysis was utilized to eliminate LiTFSI-SH (see the Experimental Section for details).

All of the proton peaks of the series of polymers were assigned in their corresponding ^{1}H and COSY NMR spectra. Figures 2 and S3 display the characteristic peaks of the protons in the polymeric backbone and side chain. Upon the introduction of the TEG group, two peaks appeared at 4.15 and 3.33 ppm, which could be ascribed to the proton, adjacent to the carbonyl group and the terminal methyl proton, respectively. Furthermore, the peaks corresponding to the allyl

https://doi.org/10.1021/acs.macromol.3c00985
Macromolecules XXXX, XXX, XXX−XXX

group at 5.81−5.11 ppm disappeared, whereas those corresponding to the $TFSI^-$ groups appeared at 3.50 and 1.34−1.07 ppm.

FT-IR spectroscopy also confirmed the introduction of each functional group (Figure 3a). In the spectra of P2 and P4, the

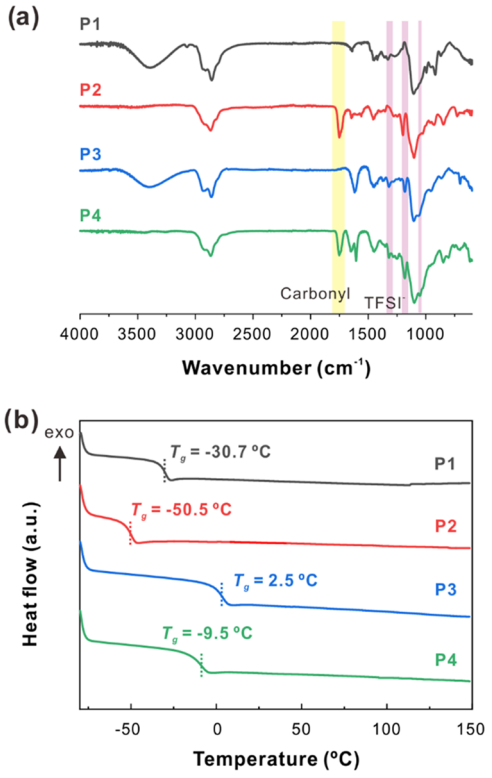

Figure 3. (a) FT-IR spectra with the assignments of characteristic peaks, such as carbonyl and $TFSI^-$ groups, and (b) DSC thermograms of P1, P2, P3, and P4 with the corresponding glass transition temperature (T_g).

stretching peak of the carbonyl group (C═O) in the TEG group was observed at 1750 cm^{-1}. Moreover, both asymmetric (1321 cm^{-1}) and symmetric (1181 cm^{-1}) stretching peaks of the SO_2 group and a stretching peak of C−F (1055 cm^{-1}), corresponding to the $TFSI^-$ anion, were observed in P3 and P4.[30,31] These results indicate that the TEG and $TFSI^-$ groups were successfully anchored to the polyether backbone. Meanwhile, the GPC results of P1 and P2 demonstrated a unimodal molecular-weight distribution, which shifted to a higher-molecular-weight region upon introduction of the TEG group (Figure S4a). P1 demonstrated an $M_{n,GPC}$ of 10,000 g mol^{-1} with a dispersity of 2.32. The molecular weight of P1 could be increased up to $M_{n,GPC}$ = 22,000 g mol^{-1} for 96 h of reaction albeit with its high dispersity of 4.40 (Figure S4b). Considering the controllable nature of the synthetic protocol, however, the reaction time for P1 was fixed at 48 h. Furthermore, the thermal properties of each polymer were confirmed by DSC and TGA measurements. According to the DSC analysis, each polymer displayed only a single T_g without melting temperature (Figure 3b), suggesting that the esterification and thiol−ene modification prevented crystallization, which resulted in the formation of an amorphous phase. In addition, the introduced TEG group decreased the T_g from 2.5 °C for P3 to −9.5 °C for P4, whereas the introduced $TFSI^-$ group increased the T_g from −50.5 °C for P2 to −9.5 °C for P4. The TGA results showed that the decomposition temperatures at 5% weight loss ($T_{d,5\%}$) were 342, 327, 243, and 258 °C for P1, P2, P3, and P4, respectively (Figure S5). The decrease in $T_{d,5\%}$ of P3 and P4 can be primarily attributed to the C−S bond, which is more thermally unstable than the C−C or C−O bond.[32] Nevertheless, the prepared polymers exhibit suitable thermal stability, indicating that these SISPEs can be safely implemented in LIBs at common operation temperatures (<100 °C). Notably, the synthesized polymers are safer than the conventional liquid electrolytes with limited thermal stability above 80 °C.[33] The representative properties of all of the polymers are summarized in Table 1. It is

Table 1. Characterizations of the Synthesized Polymers

entry	conv. (%)[a]	$M_{n,NMR}$[b] (g mol^{-1})	$M_{n,GPC}$[c] (g mol^{-1})	$Đ$	T_g[d] (°C)	$T_{d,5\%}$[e] (°C)
P1	98	8700	10,000	2.32	−30.7	342
P2	≥99	19,100	24,000	1.96	−50.5	327
P3	≥99	18,200			2.5	243
P4	≥99	28,800			−9.5	258

[a]Conversion as determined by using ^{1}H NMR spectra. [b]Determined from the ^{1}H NMR spectra of the isolated polymer (MeOD-d_4, 400 MHz). [c]Determined from GPC in DMF using an RI signal and a PMMA standard. [d]Determined by DSC at a rate of 10 °C min^{-1}. [e]Determined by TGA at a rate of 10 °C min^{-1}.

noteworthy that we evaluated the SISPE performances of only the P3 and P4 samples, which contained the $TFSI^-$ anionic group and exhibited a suitable lithium cation conductivity.

Effect of TEG Addition on Ion Transport Properties. Figure 4a shows the temperature dependence of the ionic DC conductivity, σ_{DC}, whose values are determined from the in-phase conductivity, σ' (Figure 4b), for P3 and P4. The ionic conductivity of the TEG-containing SISPE P4 (σ_{DC} = 1.7 × 10^{-6} S cm^{-1} at 60 °C) was higher than that of the SISPE without TEG, i.e., P3 (σ_{DC} = 6.7 × 10^{-9} S cm^{-1} at 60 °C). This result indicates that incorporation of the flexible polar TEG group increases σ_{DC} over the whole temperature range investigated in this study (Figure 4a). This is also consistent with the observed T_g trend, i.e., the T_g of P4 is lower than that of P3 by 12 K (Figure 3b). The temperature dependence of the ionic conductivity was fitted by the Vogel−Tammann−Fulcher (VTF) equation (eq 1)[34−38]

$$\sigma_{DC} = AT^{-1/2} \exp\left(-\frac{E_a}{R(T - T_0)}\right) \quad (1)$$

where E_a is the activation energy for ion conduction, A is the pre-exponential factor, and T_0 is the Vogel temperature; the VTF fitting parameters are summarized in Table 2, where the faster ion-conducting P4 exhibits lower E_a and T_0 than the slower ion-conducting P3. The ionic conductivities of P3 and P4 follow the VTF temperature-dependence function (Figure 4a), indicating that the ionic conductivities are strongly coupled to the segmental motion of the polymer chains.[39]

To evaluate the effect of TEG addition on σ_{DC}, which is proportional to the conducting ion mobility (μ) and conducting ion concentration (p) (i.e., $\sigma_{DC} = e\mu p$, where e is the elementary charge) in more detail,[40] an electrode polarization (EP) model was applied to the SISPEs to separate their conductivities σ_{DC} into p and μ. In the EP model, two time scales, viz. conductivity time (τ_σ) and EP time (τ_{EP}) (indicated by vertical dashed lines in Figure 4b), can be

https://doi.org/10.1021/acs.macromol.3c00985
Macromolecules XXXX, XXX, XXX−XXX

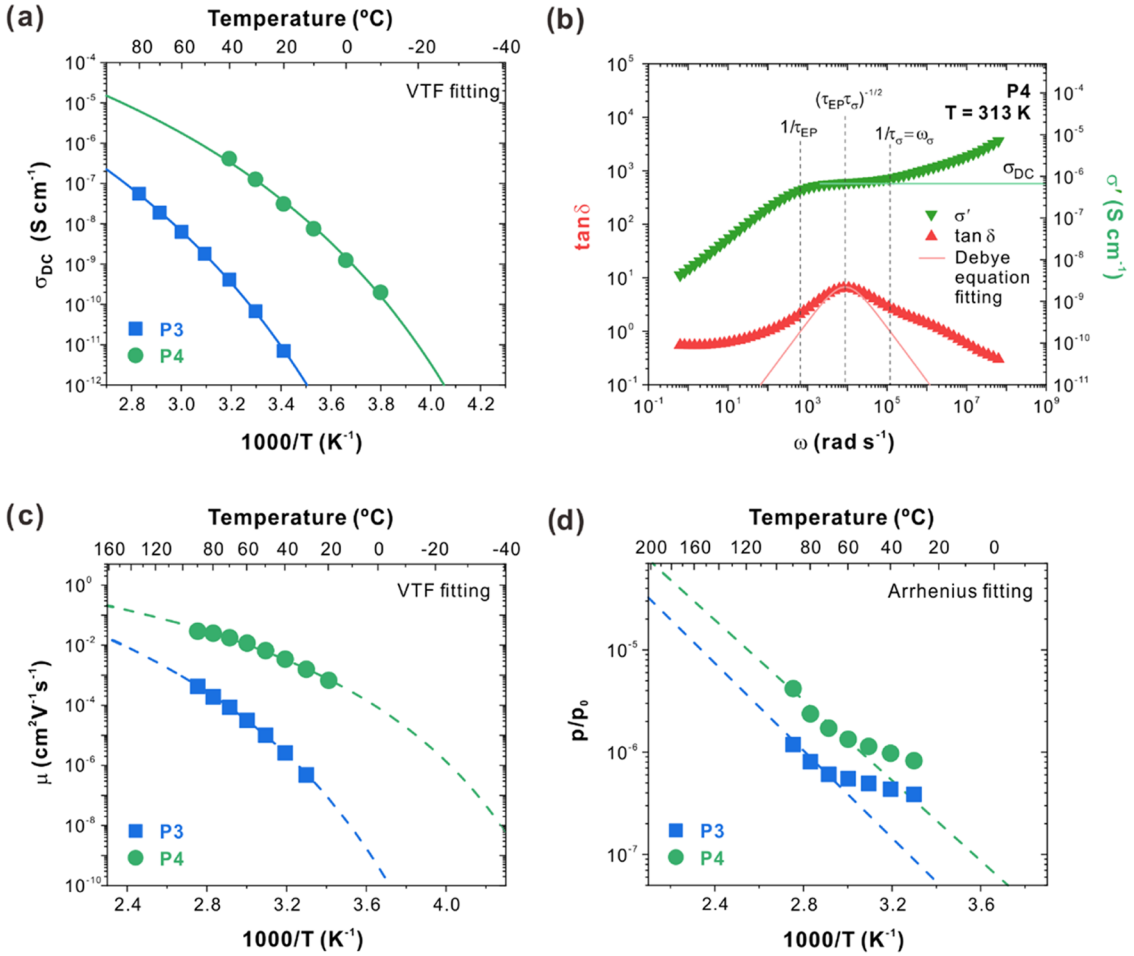

Figure 4. (a) Temperature dependence of the ionic DC conductivity (σ_{DC}) of the SISPEs (P3 and P4); the solid lines represent Vogel–Tammann–Fulcher (VTF) (eq 1) fits with fitting parameters listed in Table 2. (b) Dielectric response of P4 to an applied AC field at 313 K; loss tangent (tan δ, red symbols) and in-phase conductivity (σ', green symbols). The Debye equation (eq 2) fitted to the tan δ values (indicated by a red curve) provides the geometric mean ($(\tau_\sigma\tau_{EP})^{1/2}$) of the time scales of the conductivity (τ_σ) and electrode polarization (τ_{EP}), which determines the conducting ion concentration (p) and mobility (μ). Temperature dependence of (c) μ and (d) p/p_0, where p_0 is the total ion concentration, for P3 and P4.

Table 2. VTF Parameters for the Ionic Conductivity Data of P3 and P4

entry	A^a (S cm^{-1} K$^{-1/2}$)	$E_a{}^b$ (kJ mol^{-1})	$T_0{}^c$ (K)
P3	1.359	20.31	192
P4	0.895	14.29	180

[a]Pre-exponential factor. [b]Activation energy. [c]Vogel temperature.

obtained via a two-parameter fitting using the Debye equation for loss tan δ (red solid curve in Figure 4b)[41]

$$\tan\delta = \frac{\omega\tau_{EP}}{1 + \omega^2\tau_{EP}\tau_\sigma} \tag{2}$$

where ω is the angular frequency. According to the Coelho and Macdonald model,[42,43] the conducting ion concentration (p) and mobility (μ) can be estimated using the time scales τ_σ and τ_{EP} and the following equations[44]

$$p = \frac{(\tau_{EP})^2}{\pi l_B L^2 (\tau_\sigma)^2} \tag{3}$$

$$\mu = \frac{eL^2\tau_\sigma}{4(\tau_{EP})^2 kT} \tag{4}$$

$$l_B = \frac{e^2}{4\pi\varepsilon_s\varepsilon_0 kT} \tag{5}$$

where l_B is the Bjerrum length, L is the SISPE spacing between the blocking electrodes, ε_s is the measured static dielectric constant, k is the Boltzmann constant, T is the absolute temperature, and ε_0 is the vacuum permittivity. Figure 4c,d displays the temperature dependences of $\mu(T)$ and $p(T)$, respectively.

The following VTF equation was fitted to the $\mu(T)$ values (eq 6)[45]

$$\mu = \mu_\infty \exp\left(-\frac{DT_0}{T - T_0}\right) \tag{6}$$

where μ_∞ is the conducting ion mobility at an infinite temperature, D is the mobility strength parameter, and T_0 is the Vogel temperature. Based on the fitting parameters listed in Table 3, the VTF equation describes the SISPE mobility values well (Figure 4c). The mobility of the TEG-containing P4 sample is significantly higher than that of the TEG-free P3 sample at all of the temperatures [μ(P4) $\geq$ μ(P3)]; this result implies that TEG substitution increases the conducting ion

https://doi.org/10.1021/acs.macromol.3c00985
Macromolecules XXXX, XXX, XXX−XXX

Table 3. Characterization Data Related to Lithium-Ion Conduction in P3 and P4 Calculated from the VTF and Arrhenius Equations

entry	μ_∞ [a] ($cm^2\ V^{-1}\ s^{-1}$)	D [b]	T_0 [c] (K)	p_0 [d] (nm^{-3})	E_a^p [e] ($kJ\ mol^{-1}$)
P3	116.8	11.1	192	2.3	40.9
P4	19.1	6.4	180	1.3	37.6

[a]Conducting ion mobility at an infinite temperature. [b]Mobility strength parameter. [c]Vogel temperature. [d]Total ion concentration (estimated by the group contribution method). [e]Activation energy for conducting ions.

mobility by ≥70 times at temperatures below 90 °C. Moreover, T_0 of P4 (180 K) is lower than that of P3 (192 K), and the difference between T_g and T_0 is 84 K for both the SISPEs (Table 3). This suggests that the incorporation of TEG into SISPE accelerates segmental chain motions, leading to an increase in μ.

Figure 4d compares the fraction of Li^+ that contributes to σ_{DC} (i.e., p is normalized by p_0, which is the total cation concentration and is calculated as the reciprocal of the molecular volume obtained using the group contribution method[46] for P3 and P4). The p/p_0 value of the TEG-containing SISPE (P4) is ≥1.2 times larger than that of the TEG-free SISPE (P3) over the entire temperature range. The temperature dependence of the mobile ion concentration $p(T)$ is well described by the Arrhenius equation (eq 7 and Figure 4d)[45,47]

$$p = p_0 \exp\left(-\frac{E_a^p}{RT}\right) \tag{7}$$

where E_a^p, listed in Table 3, is the activation energy and is effectively correlated with the binding energy of an ion pair. Upon incorporation of the TEG group, the activation energy reduces from E_a^p = 40.9 kJ mol^{-1} for P3 to E_a^p = 37.6 kJ mol^{-1} for P4. This reduction in E_a^p suggests that the EO units in the TEG-containing SISPE increase the distance between the ion pairs (Li^+TFSI^-); as a result, more Li^+ participates in the ion

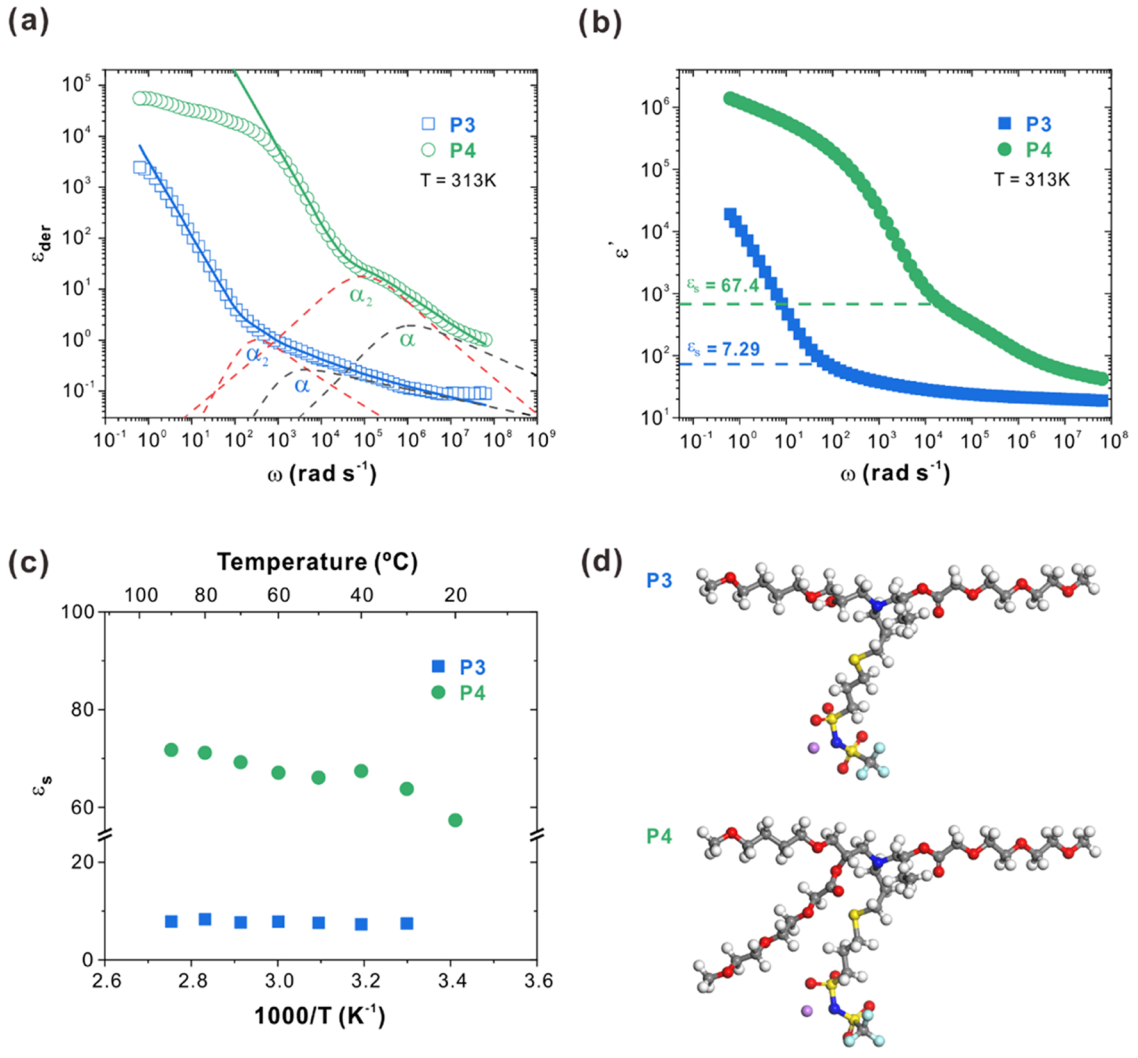

Figure 5. (a) Representative derivative spectra (ε_{der}) of P3 and P4 at 313 K; the solid lines indicate the curves fitted using a combination of a power law for EP and two derivative forms of the Havriliak–Negami (HN) function for the α_2 (red dashed line) and α (black dashed line) processes. (b) Dielectric permittivity spectra (ε') of P3 and P4 at 313 K and a comparison of their static dielectric constants (ε_s) shown by dashed lines that represent the sum of the dielectric constants of all of the observed relaxations (α and α_2 processes). (c) Temperature dependence of the static dielectric constants (ε_s) of P3 and P4. (d) Optimized configuration of the LiTFSI complex with and without the TEG group, obtained from DFT calculations.

https://doi.org/10.1021/acs.macromol.3c00985
Macromolecules XXXX, XXX, XXX−XXX

conduction with a low activation energy, unlike the case of the TEG-free SISPE (P3).

The t_{Li^+} is an important parameter for reflecting the contribution of the movement of Li^+ ions on the ionic conductivity. Therefore, to confirm the single-ion conduction properties of SISPEs, the t_{Li^+} of P4 was measured. The calculated t_{Li^+} of P4 was 0.88 at 303 K (Figure S7), which is close to unity and higher than those of dual-ion-conducting electrolytes ($t_{Li^+} < 0.5$). The parameters of the t_{Li^+} calculation for P4 are also listed in Table S2.

Dielectric Relaxation Processes and Dielectric Constant of the SISPEs. To examine the dielectric relaxation processes observed in these SISPEs, DRS measurements were performed at various temperatures and frequencies. The dipole reorientation of the chains and ions was determined from the dielectric derivative spectra[48]

$$\varepsilon_{der}(\omega) = -\frac{\pi}{2}\left[\frac{\partial\varepsilon'(\omega)}{\partial \ln \omega}\right] \tag{8}$$

in which the dipolar processes (such as segmental α or ion-rearranging α_2 relaxations) can be resolved by removing the pure-loss conductivity contribution. Figure 5a reveals the $\varepsilon_{der}(\omega)$ spectra of P3 and P4 at 313 K. The resulting dielectric derivative spectra were fitted using a power law equation for EP and two appropriate Havriliak–Negami (HN) functions for the α or α_2 processes[49,50]

$$\varepsilon_{der}^{relax} = (B\omega^{-s})_{EP} - \frac{\pi}{2}\left[\left(\frac{\partial\varepsilon'_{HN}(\omega)}{\partial \ln \omega}\right)_{\alpha_2} + \left(\frac{\partial\varepsilon'_{HN}(\omega)}{\partial \ln \omega}\right)_{\alpha}\right]$$

$$\text{with } \varepsilon'_{HN}(\omega) = \text{Real}\left\{\frac{\Delta\varepsilon}{\left[1 + \left(\frac{i\omega}{\omega_{HN}}\right)^a\right]^b}\right\} \tag{9}$$

where B and s are constant, $\Delta\varepsilon$ is the relaxation strength, a and b are shape parameters, and ω_{HN} represents the characteristic frequency related to the maximal frequency loss ω_{max}. Both P3 and P4 showed two dipolar processes, such as α and α_2 relaxations (Figure 5a). The fast α relaxation is related to the segmental motion, which involves the typical characteristics of glass transition, and the slow α_2 relaxation is attributed to the ion reorganization between the isolated and aggregated ion pairs; this ion reorganization has been similarly observed in SISPEs.[51] P4 showed the α and α_2 relaxation processes at a higher frequency compared to P3; i.e., anchoring the TEG unit to the polyether backbone accelerates the segmental motion (α), as well as the ion rearrangement (α_2). This result is consistent with the observed decrease in T_g in the DSC (Figure 3b) as well as the increase in the mobility determined from the EP analysis (Figure 4c). Thus, we can state that the TEG side chain effectively activates segmental chain motion and dissociation of conducting Li^+ from immobile $TFSI^-$.

Figure 5b displays the dielectric permittivities $\varepsilon'(\omega)$ of P3 and P4 at 313 K as a function of angular frequency. Their static dielectric constant (ε_s) values are defined as the low-frequency plateau of $\varepsilon'(\omega)$ before the onset of EP and are determined from the sum of the dielectric constants of all of the observed relaxations (such as the α and α_2 processes) and the high-frequency limit of the dielectric constant ε_∞ as follows (eq 10)[48,51]

$$\varepsilon_s \approx \lim_{\omega\to\infty}[\varepsilon'_{\alpha_2}(\omega) + \varepsilon'_{\alpha}(\omega)] + \varepsilon_\infty \tag{10}$$

Figure 5c compares the temperature dependences of ε_s for P3 and P4. TEG side-chain incorporation in the backbone leads to a substantial increase in ε_s, i.e., $\varepsilon_s = 64$ for P4 and $\varepsilon_s = 7$ for P3 at 303 K. The ε_s value of P4 is nearly equivalent to that of propylene carbonate (65 at 298 K).[52,53] The TEG side-chain insertion results in an enhancement of ε_s over the whole temperature range. Because the EO unit in the TEG group interacts with Li^+ via ion–dipole interactions, the Li^+–O_{EO} interaction can reduce the ion-pair dissociation energy of Li^+TFSI^-. This can be supported by DFT calculations, demonstrating that the binding energy of Li^+TFSI^- in P4 (-591.72 kJ mol^{-1}) is smaller in magnitude than that in P3 (-597.11 kJ mol^{-1}) and suggesting that TEG weakens the Li^+TFSI^- interactions. The DFT-optimized structures of P3 and P4 are illustrated in Figure 5d. Therefore, this TEG group effectively stabilizes Li^+ separated from $TFSI^-$, and as a result, quadrupole $[(Li^+TFSI^-)_2]$ with nearly zero dipole moments can separate into individual ion pairs (Li^+TFSI^-). This complexation assists the Li^+ countercations to move farther away from the $TFSI^-$ anions, thereby increasing the average distance between Li^+ and $TFSI^-$ in the ion pair (creating a separated ion pair). Because of the Li^+–O_{EO} complex formation, the dipole moment of the separated ion pair (m_{pair}) becomes larger than that of the contact ion pair and the number density of the ion pair (ν_{pair}) increases, instead of that of the quadrupoles.

This mechanism is responsible for the observed increase in the static dielectric constant upon TEG side-chain substitution (predicted by the Onsager equation: $\varepsilon_s \sim m_{pair}^2\nu_{pair}$) and is responsible for the observed increase in the conducting ion concentration (p, Figure 4d) and mobility (μ, Figure 4c); these increased p and μ values are responsible for the increased conductivity (σ_{DC}, Figure 4a) of the TEG-incorporated sample. The Onsager equation used to fit the static dielectric constant values of P3 and P4 is presented below (eq 11)[47,54]

$$\frac{(\varepsilon_s - \varepsilon_\infty)(2\varepsilon_s + \varepsilon_\infty)}{\varepsilon_s(\varepsilon_\infty + 2)^2} = \frac{Nm^2}{9\varepsilon_0 kT} \tag{11}$$

where ε_∞ is the high-frequency limit of the dielectric constant, N and m are the number density and dipole moment of the Li^+TFSI^- dipole, respectively, and ε_0 is vacuum permittivity. For P3 and P4, we calculated m = 3.63 and 14.1 D, respectively, using the Onsager equation based on the data, and these determined m values confirm that the dipole moment increases with the introduction of the TEG group. Because the introduced TEG group suppresses ion-pair aggregation (Li^+TFSI^-), the dipole moment m of P4 is higher than that of P3. Nevertheless, the low conductivities of these SISPEs imply that all Li^+ cannot participate in conduction, because of the ion correlation in the ion-rich domains.

Effect of SN Additive on the Ionic Conductivities of the SISPEs. To further enhance the ionic conductivity of the SISPEs, a plasticizer, SN, was blended with P4. When the plastic crystal SN was added to P4, the ionic conductivity further increased, and the maximum enhancement of σ_{DC} was observed at 10 wt % of SN content (1.8×10^{-5} S cm^{-1} at 60 °C); this σ_{DC} value is 1 order of magnitude higher than that of the neat P4. However, a further increase in the SN content (55 wt %) resulted in only a marginal decrease in the conductivity, which may be attributed to the inactive SN; this inactive SN

https://doi.org/10.1021/acs.macromol.3c00985
Macromolecules XXXX, XXX, XXX–XXX

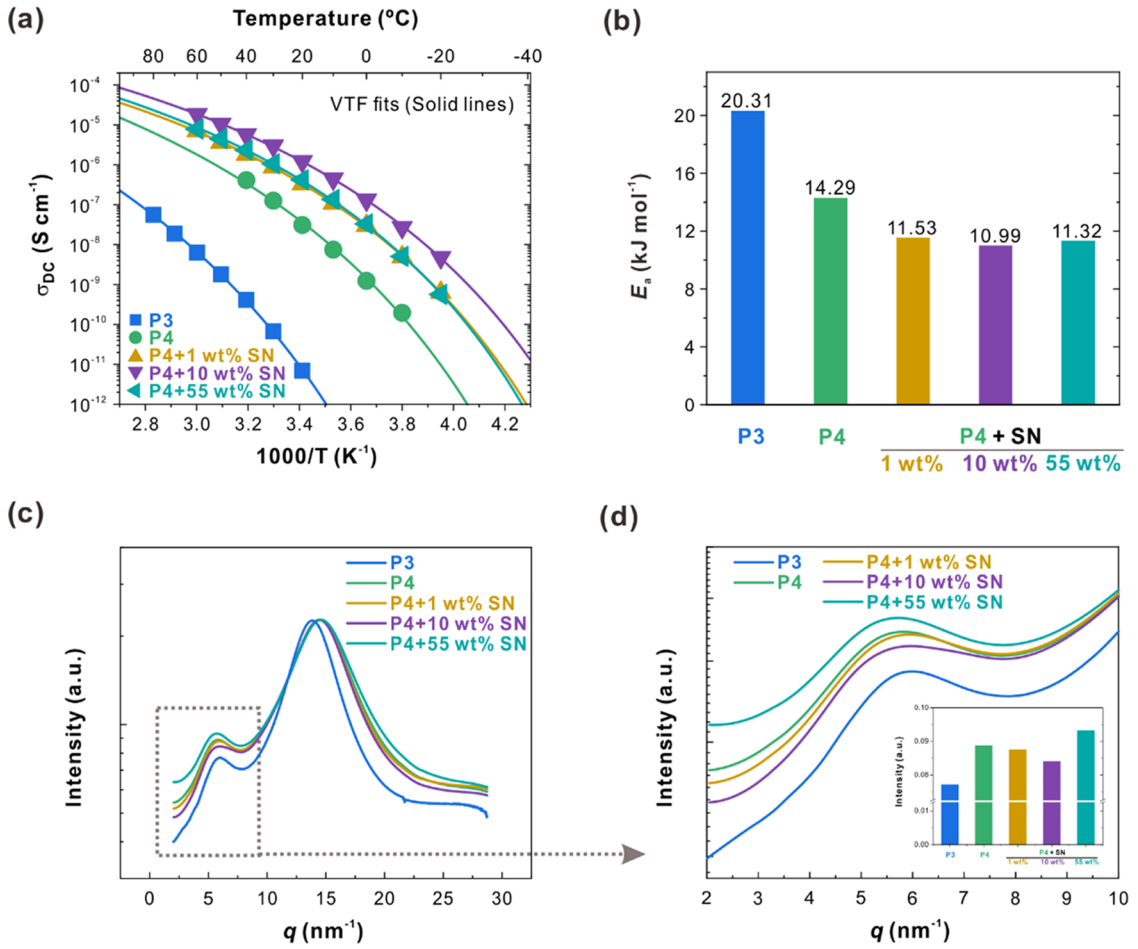

Figure 6. (a) VTF plots of the ionic conductivity of P3, P4, and P4 blend with SN (P4 + *X* wt % SN, where *X* = 1, 10, and 55). (b) Activation energy for lithium-ion conduction of the SISPEs; the values are calculated using the VTF equation. (c) WAXS data of P3, P4, and P4 blend with SN (P4 + *X* wt % SN, where *X* = 1, 10, and 55) at 25 °C and (d) their magnification at low *q* ranges, with the inset showing the intensity of scattering peak of ionic aggregates at $q = \sim 5.7$ nm^{-1}.

acted as an insulator and hindered the conduction of Li^+.[55] The activation energy calculated through VTF fitting showed an identical trend with the ionic conductivity (Figure 6a,b). The activation energies of P3 and P4 were determined to be 20.31 and 14.29 kJ mol^{-1}, respectively, which decreased with the introduction of the TEG group. Furthermore, when P4 was blended with SN, the minimum activation energy (10.99 kJ mol^{-1}) was observed at 10 wt %, which then increased to 11.32 kJ mol^{-1} when the SN content was increased to 55 wt % in the P4−SN blend.

Meanwhile, to investigate the plasticizing effect of SN in the P4−SN blend, the thermal properties were examined through DSC measurements, and it was observed that T_g tended to decrease with increasing SN content (Figure S9a). Furthermore, the ionic conductivity with T_g/T was plotted to obtain clearer insights into the effect of SN on the segmental dynamics in ion transport (Figure S9b). According to previous reports, ionic motion is strongly associated with segmental dynamics when the ionic conductivity at T_g is in the order of 10^{-14}−10^{-15} S cm^{-1}.[56,57] The ionic conductivity at T_g higher than 10^{-14} suggests that the ionic motion is faster than segmental dynamics. In this study, the ionic conductivity at T_g of P3 is 5.4×10^{-14} S cm^{-1}, indicating that the ionic motion is strongly associated with segmental dynamics. When the TEG side chain is included, the ionic conductivity at T_g for P4 is increased sharply to 1.85×10^{-10} S cm^{-1}, indicating that ionic motion is faster than segmental dynamics consistent with the DRS results. Furthermore, the P4−SN blends exhibit a higher ionic mobility, with ionic conductivities at T_g exceeding 2 orders of magnitude higher than 10^{-14} S cm^{-1}.

WAXS measurements were performed to investigate the effect of the SN additive as a plasticizer on the molecular correlations (Figure 6c,d), which were associated with the ionic conductivity of the prepared electrolytes. The scattering profiles were vertically shifted to normalize them by superimposing the amorphous halo located at $q = 14$ nm^{-1}, which originated from the intrachain pendant spacing.[57,58] The scattering peaks at $q = 5.7$ nm^{-1} in the spectra of P4 and P4−SN blends correspond to the spacing between ionic aggregates.[58−60] In addition, the spacing between the ionic aggregates was calculated to be $2\pi/q = 1.1$ nm according to Bragg's law.[57,58] The observed decrease in the peak intensity upon the addition of 10 wt % of SN suggests that the plasticizing effect of SN strongly suppresses the ionic aggregation. In contrast, the P4 + 55 wt % SN blend exhibited an increased peak intensity, which can be attributed to crystallization by the excess SN; this crystallization results in a poor plasticizing effect.[61] Meanwhile, the scattering peak originating from ionic aggregates of P3 ($q = 6.0$ nm^{-1}) was detected at higher *q* and lower intensity compared to P4 and

https://doi.org/10.1021/acs.macromol.3c00985
Macromolecules XXXX, XXX, XXX−XXX

P4−SN blends, suggesting the relatively weaker periodicity of ionic aggregates due to hydrogen bonding by hydroxyl groups. From the WAXS results of P1 and P2 without $TFSI^-$ pendant (Figure S10), the scattering peak of interchain hydrogen bond between adjacent hydroxyl groups was observed at q = 6.4 nm^{-1}.[62,63] The scattering peaks of ionic aggregates were observed at lower q compared to the scattering peaks from interchain hydrogen bonds because the large size and delocalization of the negative charge of $TFSI^-$ make ionic aggregation less periodic than interchain hydrogen bonding. In addition, for P2, the interchain correlation by hydrogen bonds was weakened due to the TEG chain located proximity to the hydroxyl group.

Taken together with the results from impedance spectroscopy, DRS, and WAXS analyses, the lithium-ion conduction mechanism in SISPEs is predicted as illustrated in Figure 7;

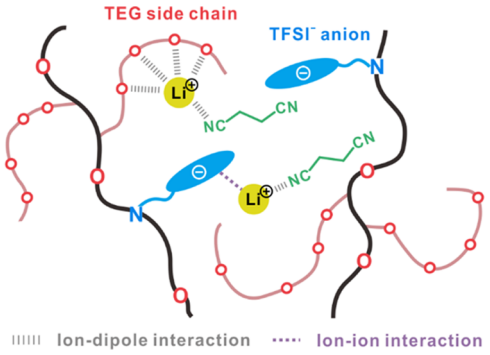

Figure 7. Proposed Li^+ conduction mechanism in the blend of P4 with SN.

(1) The Li^+ cations, electrostatically bound to the $TFSI^-$ counteranion, easily dissociate because of the delocalized negative charge of the $TFSI^-$ counteranion. (2) The TEG group lowers the T_g and enhances the segmented motion, thereby accelerating the transport of Li^+. The Li^+ cations are readily coordinated by several oxygen atoms of the TEG side chain. (3) The plasticizing effect of SN improves the transport of Li^+.

CONCLUSIONS

We developed polyether-based SISPEs by exploiting the polymer backbone to introduce diverse functional moieties through orthogonal functionalization. The polymer backbone containing allyl and hydroxyl groups was functionalized with the $TFSI^-$ and TEG groups. The introduction of the TEG group improved the segmental motion of the SISPEs, leading to the improvement of ionic conductivity, e.g., a ∼250-fold increase at 60 °C. Furthermore, the incorporation of the plasticizer SN into the SISPE also enhanced the ionic conductivity up to 1.8×10^{-5} S cm^{-1} at 60 °C. DSC, DRS, and WAXS analyses revealed that the addition of TEG lowered T_g and enhanced the segmental motion of the SISPEs; as a result, fast α and α_2 relaxations and an increased static dielectric constant were observed. Moreover, the SN additive suppressed ion−ion correlations by promoting ion-pair dissociation. This study presents the platform of SISPEs, whose properties can be readily tailorable by introducing various functional groups.

ASSOCIATED CONTENT

Supporting Information

The Supporting Information is available free of charge at https://pubs.acs.org/doi/10.1021/acs.macromol.3c00985.

Synthetic procedures of SISPEs and LiTFSI-SH; additional analysis including ^{1}H, COSY, GPC, TGA, and impedance spectroscopy data; VFT parameters for the ionic conductivity data of P3, P4, and P4−SN blends; lithium transference number (t_{Li^+}) of P4; ionic conductivity at 303 K for P4 and P4 blends; DSC thermograms of P4 and P4 blends; and WAXS data of P1, P2, P3, and P4 (PDF)

AUTHOR INFORMATION

Corresponding Authors

U Hyeok Choi − *Department of Polymer Science and Engineering and Program in Environmental and Polymer Engineering, Inha University, Incheon 22212, Republic of Korea;* orcid.org/0000-0002-0048-9550; Email: uhyeok@inha.ac.kr

Byeong-Su Kim − *Department of Chemistry, Yonsei University, Seoul 03722, Republic of Korea;* orcid.org/0000-0002-6419-3054; Email: bskim19@yonsei.ac.kr

Authors

Jiyoung Lee − *Department of Chemistry, Yonsei University, Seoul 03722, Republic of Korea*

Seonho Kim − *Department of Polymer Science and Engineering and Program in Environmental and Polymer Engineering, Inha University, Incheon 22212, Republic of Korea;* orcid.org/0000-0003-2466-5771

Hyeoksu Kwon − *Department of Polymer Science and Engineering and Program in Environmental and Polymer Engineering, Inha University, Incheon 22212, Republic of Korea*

Seungyun Jo − *Department of Chemical and Biomolecular Engineering, Yonsei University, Seoul 03722, Republic of Korea*

Du Yeol Ryu − *Department of Chemical and Biomolecular Engineering, Yonsei University, Seoul 03722, Republic of Korea;* orcid.org/0000-0002-0929-7934

Complete contact information is available at: https://pubs.acs.org/10.1021/acs.macromol.3c00985

Notes

The authors declare no competing financial interest.

ACKNOWLEDGMENTS

This work was supported by the National Research Foundation of Korea (NRF-2021R1A2C3004978 and NRF-2022R1F1A1069348) and Institute of Convergence Science (ICONS) of Yonsei University.

REFERENCES

(1) Liu, Y.-K.; Zhao, C.-Z.; Du, J.; Zhang, X.-Q.; Chen, A.-B.; Zhang, Q. Research Progresses of Liquid Electrolytes in Lithium-Ion Batteries. *Small* **2023**, *19*, No. 2205315.

(2) Francis, C. F. J.; Kyratzis, I. L.; Best, A. S. Lithium-Ion Battery Separators for Ionic-Liquid Electrolytes: A Review. *Adv. Mater.* **2020**, *32*, No. 1904205.

(3) Zhao, C.-Z.; Zhao, B.-C.; Yan, C.; Zhang, X.-Q.; Huang, J.-Q.; Mo, Y.; Xu, X.; Li, H.; Zhang, Q. Liquid Phase Therapy to Solid

Electrolyte−Electrode Interface in Solid-State Li Metal Batteries: A review. *Energy Storage Mater.* **2020**, *24*, 75−84.
(4) Seki, S.; Hayamizu, K.; Tsuzuki, S.; Takahashi, K.; Ishino, Y.; Kato, M.; Nozaki, E.; Watanabe, H.; Umebayashi, Y. Density, Viscosity, Ionic Conductivity, and Self-Diffusion Coefficient of Organic Liquid Electrolytes: Part I. Propylene Carbonate + Li, Na, Mg and Ca Cation Salts. *J. Electrochem. Soc.* **2018**, *165*, A542.
(5) Gauthier, M.; Carney, T. J.; Grimaud, A.; Giordano, L.; Pour, N.; Chang, H.-H.; Fenning, D. P.; Lux, S. F.; Paschos, O.; Bauer, C.; Maglia, F.; Lupart, S.; Lamp, P.; Shao-Horn, Y. Electrode−Electrolyte Interface in Li-Ion Batteries: Current Understanding and New Insights. *J. Phys. Chem. Lett.* **2015**, *6*, 4653−4672.
(6) Seidl, L.; Martens, S.; Ma, J.; Stimming, U.; Schneider, O. In Situ Scanning Tunneling Microscopy Studies of the SEI Formation on Graphite Electrodes for Li^+-ion batteries. *Nanoscale* **2016**, *8*, 14004−14014.
(7) Liu, K.; Liu, Y.; Lin, D.; Pei, A.; Cui, Y. Materials for Lithium-Ion Battery Safety. *Sci. Adv.* **2018**, *4*, No. eaas9820.
(8) Li, S.; Zhang, S.-Q.; Shen, L.; Liu, Q.; Ma, J.-B.; Lv, W.; He, Y.-B.; Yang, Q.-H. Progress and Perspective of Ceramic/Polymer Composite Solid Electrolytes for Lithium Batteries. *Adv. Sci.* **2020**, *7*, No. 1903088.
(9) Zhou, D.; Shanmukaraj, D.; Tkacheva, A.; Armand, M.; Wang, G. Polymer Electrolytes for Lithium-Based Batteries: Advances and Prospects. *Chem* **2019**, *5*, 2326−2352.
(10) Zhao, Y.; Wang, L.; Zhou, Y.; Liang, Z.; Tavajohi, N.; Li, B.; Li, T. Solid Polymer Electrolytes with High Conductivity and Transference Number of Li Ions for Li-Based Rechargeable Batteries. *Adv. Sci.* **2021**, *8*, No. 2003675.
(11) Stolz, L.; Röser, S.; Homann, G.; Winter, M.; Kasnatscheew, J. Pragmatic Approaches to Correlate between the Physicochemical Properties of a Linear Poly(ethylene oxide)-Based Solid Polymer Electrolyte and the Performance in a High-Voltage Li-Metal Battery. *J. Phys. Chem. C* **2021**, *125*, 18089−18097.
(12) Stolz, L.; Homann, G.; Winter, M.; Kasnatscheew, J. The Sand Equation and Its Enormous Practical Relevance for Solid-State Lithium Metal Batteries. *Mater. Today* **2021**, *44*, 9−14.
(13) Gao, J.; Wang, C.; Han, D.-W.; Shin, D.-M. Single-Ion Conducting Polymer Electrolytes as a Key Jigsaw Piece for Next-Generation Battery Applications. *Chem. Sci.* **2021**, *12*, 13248−13272.
(14) Jeong, K.; Park, S.; Lee, S.-Y. Revisiting Polymeric Single Lithium-Ion Conductors as an Organic Route for All-Solid-State Lithium Ion and Metal Batteries. *J. Mater. Chem. A* **2019**, *7*, 1917−1935.
(15) Meziane, R.; Bonnet, J.-P.; Courty, M.; Djellab, K.; Armand, M. Single-Ion Polymer Electrolytes Based on a Delocalized Polyanion for Lithium Batteries. *Electrochim. Acta* **2011**, *57*, 14−19.
(16) Bouchet, R.; Maria, S.; Meziane, R.; Aboulaich, A.; Lienafa, L.; Bonnet, J.-P.; Phan, T. N. T.; Bertin, D.; Gigmes, D.; Devaux, D.; Denoyel, R.; Armand, M. Single-Ion BAB Triblock Copolymers as Highly Efficient Electrolytes for Lithium-Metal Batteries. *Nat. Mater.* **2013**, *12*, 452−457.
(17) Xue, Z.; He, D.; Xie, X. Poly(Ethylene Oxide)-Based Electrolytes for Lithium-Ion Batteries. *J. Mater. Chem. A* **2015**, *3*, 19218−19253.
(18) Armand, M. Polymers with Ionic Conductivity. *Adv. Mater.* **1990**, *2*, 278−286.
(19) Bresser, D.; Lyonnard, S.; Iojoiu, C.; Picard, L.; Passerini, S. Decoupling Segmental Relaxation and Ionic Conductivity for Lithium-Ion Polymer Electrolytes. *Mol. Syst. Des. Eng.* **2019**, *4*, 779−792.
(20) Glynos, E.; Pantazidis, C.; Sakellariou, G. Designing All-Polymer Nanostructured Solid Electrolytes: Advances and Prospects. *ACS Omega* **2020**, *5*, 2531−2540.
(21) Johansson, P.; Tegenfeldt, J.; Lindgren, J. Modelling Lithium Ion Transport in Helical PEO by Ab Initio Calculations. *Polymer* **2001**, *42*, 6573−6577.
(22) Kim, B.; Chae, C.-G.; Satoh, Y.; Isono, T.; Ahn, M.-K.; Min, C.-M.; Hong, J.-H.; Ramirez, C. F.; Satoh, T.; Lee, J.-S. Synthesis of Hard−Soft−Hard Triblock Copolymers, Poly(2-naphthyl glycidyl ether)-block-poly[2-(2-(2-methoxyethoxy)ethoxy)ethyl glycidyl ether]-block-poly(2-naphthyl glycidyl ether), for Solid Electrolytes. *Macromolecules* **2018**, *51*, 2293−2301.
(23) Butzelaar, A. J.; Liu, K. L.; Röring, P.; Brunklaus, G.; Winter, M.; Theato, P. A Systematic Study of Vinyl Ether-Based Poly(Ethylene Oxide) Side-Chain Polymer Electrolytes. *ACS Appl. Polym. Mater.* **2021**, *3*, 1573−1582.
(24) Krimalowski, A.; Thelakkat, M. Sequential Co-Click Reactions with Poly(glycidyl propargyl ether) toward Single-Ion Conducting Electrolytes. *Macromolecules* **2019**, *52*, 4042−4051.
(25) Guzmán-González, G.; Vauthier, S.; Alvarez-Tirado, M.; Cotte, S.; Castro, L.; Guéguen, A.; Casado, N.; Mecerreyes, D. Single-Ion Lithium Conducting Polymers with High Ionic Conductivity Based on Borate Pendant Groups. *Angew. Chem., Int. Ed.* **2022**, *61*, No. e202114024.
(26) Perdew, J. P.; Burke, K.; Ernzerhof, M. Generalized Gradient Approximation Made Simple. *Phys. Rev. Lett.* **1996**, *77*, 3865−3868.
(27) Saha, A.; De, S.; Stuparu, M. C.; Khan, A. Facile and General Preparation of Multifunctional Main-Chain Cationic Polymers through Application of Robust, Efficient, and Orthogonal Click Chemistries. *J. Am. Chem. Soc.* **2012**, *134*, 17291−17297.
(28) Hatakeyama-Sato, K.; Kimura, S.; Matsumoto, S.; Oyaizu, K. Facile Synthesis of Poly(glycidyl ether)s with Ionic Pendant Groups by Thiol-Ene Reactions. *Macromol. Rapid Commun.* **2020**, *41*, No. 1900399.
(29) Baille, W. E.; Malveau, C.; Zhu, X. X.; Kim, Y. H.; Ford, W. T. Self-Diffusion of Hydrophilic Poly(propyleneimine) Dendrimers in Poly(vinyl alcohol) Solutions and Gels by Pulsed Field Gradient NMR Spectroscopy. *Macromolecules* **2003**, *36*, 839−847.
(30) Porcarelli, L.; Shaplov, A. S.; Salsamendi, M.; Nair, J. R.; Vygodskii, Y. S.; Mecerreyes, D.; Gerbaldi, C. Single-Ion Block Copoly(ionic liquid)s as Electrolytes for All-Solid State Lithium Batteries. *ACS Appl. Mater. Interfaces* **2016**, *8*, 10350−10359.
(31) Lingua, G.; Grysan, P.; Vlasov, P. S.; Verge, P.; Shaplov, A. S.; Gerbaldi, C. Unique Carbonate-Based Single Ion Conducting Block Copolymers Enabling High-Voltage, All-Solid-State Lithium Metal Batteries. *Macromolecules* **2021**, *54*, 6911−6924.
(32) Soeriyadi, A. H.; Li, G.-Z.; Slavin, S.; Jones, M. W.; Amos, C. M.; Becer, C. R.; Whittaker, M. R.; Haddleton, D. M.; Boyer, C.; Davis, T. P. Synthesis and Modification of Thermoresponsive Poly(oligo(ethylene glycol) methacrylate) via Catalytic Chain Transfer Polymerization and Thiol−Ene Michael Addition. *Polym. Chem.* **2011**, *2*, 815−822.
(33) Reiter, J.; Dominko, R.; Nádherná, M.; Jakubec, I. Ion-Conducting Lithium Bis(oxalato)borate-Based Polymer Electrolytes. *J. Power Sources* **2009**, *189*, 133−138.
(34) Vogel, H. The Law of the Relation between the Viscosity of Liquids and the Temperature. *Phys. Z* **1921**, *22*, 645−646.
(35) Fulcher, G. S. Analysis of Recent Measurements of the Viscosity of Glasses. *J. Am. Ceram. Soc.* **1925**, *8*, 339−355.
(36) Tammann, G.; Hesse, W. The Dependence of Viscosity upon the Temperature of Supercooled Liquids. *Z. Anorg. Allg. Chem.* **1926**, *156*, 245−257.
(37) Angell, C. A. Free Volume Model for Transport in Fused Salts: Electrical Conductance in Glass-Forming Nitrate Melts. *J. Phys. Chem. A* **1964**, *68*, 1917−1929.
(38) Jang, H. K.; Jung, B. M.; Choi, U. H.; Lee, S. B. Ion Conduction and Viscoelastic Response of Epoxy-Based Solid Polymer Electrolytes Containing Solvating Plastic Crystal Plasticizer. *Macromol. Chem. Phys.* **2018**, *219*, No. 1700514.
(39) Gu, G. Y.; Bouvier, S.; Wu, C.; Laura, R.; Rzeznik, M.; Abraham, K. M. 2-Methoxyethyl (methyl) Carbonate-Based Electrolytes for Li-ion Batteries. *Electrochim. Acta* **2000**, *45*, 3127−3139.
(40) Tu, C.-H.; Veith, L.; Butt, H.-J.; Floudas, G. Ionic Conductivity of a Solid Polymer Electrolyte Confined in Nanopores. *Macromolecules* **2022**, *55*, 1332−1341.
(41) Jangu, C.; Wang, J.-H. H.; Wang, D.; Sharick, S.; Heflin, J. R.; Winey, K. I.; Colby, R. H.; Long, T. E. Well-Defined Imidazolium

https://doi.org/10.1021/acs.macromol.3c00985
Macromolecules XXXX, XXX, XXX−XXX

ABA Triblock Copolymers as Ionic-Liquid-Containing Electroactive Membranes. *Macromol. Chem. Phys.* **2014**, *215*, 1319−1331.
(42) Klein, R. J.; Zhang, S.; Dou, S.; Jones, B. H.; Colby, R. H.; Runt, J. Modeling Electrode Polarization in Dielectric Spectroscopy: Ion Mobility and Mobile Ion Concentration of Single-Ion Polymer Electrolytes. *J. Chem. Phys.* **2006**, *124*, No. 144903.
(43) Sen, S.; Zhu, H.; Forsyth, M.; Bhattacharyya, A. J. Time−Temperature Scaling and Dielectric Modeling of Conductivity Spectra of Single-Ion Conducting Liquid Dendrimer Electrolytes. *J. Phys. Chem. B* **2019**, *123*, 207−215.
(44) Lee, M.; Choi, U. H.; Colby, R. H.; Gibson, H. W. Ion Conduction in Imidazolium Acrylate Ionic Liquids and their Polymers. *Chem. Mater.* **2010**, *22*, 5814−5822.
(45) Fragiadakis, D.; Dou, S.; Colby, R. H.; Runt, J. Molecular Mobility, Ion Mobility, and Mobile Ion Concentration in Poly(ethylene oxide)-Based Polyurethane Ionomers. *Macromolecules* **2008**, *41*, 5723−5728.
(46) Van Krevelen, D. W.; te Nijenhuis, K. *Properties of Polymers*; Elsevier: Amsterdam, 2009.
(47) Fragiadakis, D.; Dou, S.; Colby, R. H.; Runt, J. Molecular Mobility and Li^+ Conduction in Polyester Copolymer Ionomers Based on Poly(ethylene oxide). *J. Chem. Phys.* **2009**, *130*, No. 064907.
(48) Choi, U. H.; Mittal, A.; Price, T. L., Jr.; Gibson, H. W.; Runt, J.; Colby, R. H. Polymerized Ionic Liquids with Enhanced Static Dielectric Constants. *Macromolecules* **2013**, *46*, 1175−1186.
(49) Havriliak, S.; Negami, S. A Complex Plane Representation of Dielectric and Mechanical Relaxation Processes in Some Polymers. *Polymer* **1967**, *8*, 161−210.
(50) Kremer, F.; Schönhals, A. *Broadband Dielectric Spectroscopy*; Springer Science & Business Media, 2002.
(51) Choi, U. H.; Price, T. L., Jr.; Schoonover, D. V.; Gibson, H. W.; Colby, R. H. The Effect of Oligo(oxyethylene) Moieties on Ion Conduction and Dielectric Properties of Norbornene-Based Imidazolium Tf_2N Ionic Liquid Monomers. *Macromolecules* **2020**, *53*, 4990−5000.
(52) Choi, U. H.; Liang, S.; Chen, Q.; Runt, J.; Colby, R. H. Segmental Dynamics and Dielectric Constant of Polysiloxane Polar Copolymers as Plasticizers for Polymer Electrolytes. *ACS Appl. Mater. Interfaces* **2016**, *8*, 3215−3225.
(53) Xu, K. Nonaqueous Liquid Electrolytes for Lithium-Based Rechargeable Batteries. *Chem. Rev.* **2004**, *104*, 4303−4418.
(54) Onsager, L. Electric Moments of Molecules in Liquids. *J. Am. Chem. Soc.* **1936**, *58*, 1486−1493.
(55) Fan, L.-Z.; Hu, Y.-S.; Bhattacharyya, A. J.; Maier, J. Succinonitrile as a Versatile Additive for Polymer Electrolytes. *Adv. Funct. Mater.* **2007**, *17*, 2800−2807.
(56) Stacy, E. W.; Gainaru, C. P.; Gobet, M.; Wojnarowska, Z.; Bocharova, V.; Greenbaum, S. G.; Sokolov, A. P. Fundamental Limitations of Ionic Conductivity in Polymerized Ionic Liquids. *Macromolecules* **2018**, *51*, 8637−8645.
(57) Paren, B. A.; Nguyen, N.; Ballance, V.; Hallinan, D. T.; Kennemur, J. G.; Winey, K. I. Superionic Li-Ion Transport in a Single-Ion Conducting Polymer Blend Electrolyte. *Macromolecules* **2022**, *55*, 4692−4702.
(58) Mei, W.; Yu, D.; George, C.; Madsen, L. A.; Hickey, R. J.; Colby, R. H. Anion Chemical Composition of Poly(ethylene oxide)-Based Sulfonylimide and Sulfonate Lithium Ionomers Controls Ion Aggregation and Conduction. *J. Mater. Chem. C* **2022**, *10*, 14569−14579.
(59) Wang, J.-H. H.; Yang, C. H.-C.; Masser, H.; Shiau, H.-S.; O'Reilly, M. V.; Winey, K. I.; Runt, J.; Painter, P. C.; Colby, R. H. Ion States and Transport in Styrenesulfonate Methacrylic PEO9 Random Copolymer Ionomers. *Macromolecules* **2015**, *48*, 7273−7285.
(60) Hall, L. M.; Seitz, M. E.; Winey, K. I.; Opper, K. L.; Wagener, K. B.; Stevens, M. J.; Frischknecht, A. L. Ionic Aggregate Structure in Ionomer Melts: Effect of Molecular Architecture on Aggregates and the Ionomer Peak. *J. Am. Chem. Soc.* **2012**, *134*, 574−587.
(61) Pal, P.; Ghosh, A. Robust Succinonitrile Plastic Crystal-Based Ionogel for All-Solid-State Li-Ion and Dual-Ion Batteries. *ACS Appl. Energy Mater.* **2020**, *3*, 4295−4304.
(62) Watanabe, T.; Terada, K.; Takemura, S.; Masunaga, H.; Tsuchiya, K.; Lamprou, A.; Numata, K. Chemoenzymatic Polymerization of l-Serine Ethyl Ester in Aqueous Media without Side-Group Protection. *ACS Polym. Au* **2022**, *2*, 147−156.
(63) Katz, J. R. X-ray Spectrography of Polymers and in Particular those having a Rubber-Like Extensibility. *Trans. Faraday Soc.* **1936**, *32*, 77−94.

https://doi.org/10.1021/acs.macromol.3c00985
Macromolecules XXXX, XXX, XXX−XXX